**Showcasing collaborative research work from Prof. V. M. Murukeshan's group at the Centre for Optical and Laser Engineering (COLE), Nanyang Technological University, Singapore; Prof. C. Vijayan's group at the Photonics laboratory, Department of Physics, Indian Institute of Technology Madras, India; Prof. Balázs Gulyás's group at the Cognitive Neuroimaging Centre (CONIC) and Dr Parasuraman Padmanabhan at the Imaging Probe Development Platform (IPDP) at LKC Medicine, Nanyang Technological University, Singapore.**

Plasmonic random laser enabled artefact-free wide-field fluorescence bioimaging: uncovering finer cellular features

An exemplary, artefact-free, wide-field fluorescence bioimaging modality based on spatially incoherent plasmonic random laser is proposed and demonstrated for the first time. The developed system offers distinct advantages such as artefact-free imaging, efficient and specific fluorophore excitation, low photo bleaching, high contrast imaging and opens up possibilities for real-time, *in vivo* fluorescence bioimaging.

As featured in:
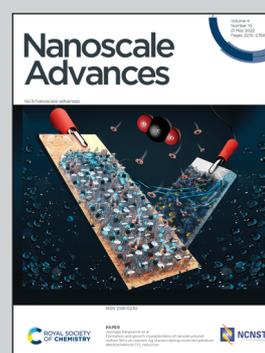
See R. Gayathri *et al.*,
Nanoscale Adv., 2022, **4**, 2278.

Nanoscale Advances

PAPER

Check for updates

Plasmonic random laser enabled artefact-free wide-field fluorescence bioimaging: uncovering finer cellular features†

R. Gayathri, [ID] ‡[ab] C. S. Suchand Sandeep, [ID] ‡[a] V. S. Gummaluri, [ID] [a] R. Mohamed Asik, [ID] [cd] Parasuraman Padmanabhan,*[ce] Balázs Gulyás,[cef] C. Vijayan*[b] and V. M. Murukeshan*[a]

Narrow bandwidth, high brightness, and spectral tunability are the unique properties of lasers that make them extremely desirable for fluorescence imaging applications. However, due to the high spatial coherence, conventional lasers are often incompatible for wide-field fluorescence imaging. The presence of parasitic artefacts under coherent illumination causes uneven excitation of fluorophores, which has a critical impact on the reliability, resolution, and efficiency of fluorescence imaging. Here, we demonstrate artefact-free wide-field fluorescence imaging with a bright and low threshold silver nanorod based plasmonic random laser, offering the capability to image finer cellular features with sub-micrometer resolution even in highly diffusive biological samples. A spatial resolution of 454 nm and up to 23% enhancement in the image contrast in comparison to conventional laser illumination are attained. Based on the results presented in this paper, random lasers, with their laser-like properties and spatial incoherence are envisioned to be the next-generation sources for developing highly efficient wide-field fluorescence imaging systems having high spatial and temporal resolution for real-time, *in vivo* bioimaging.

Introduction

Fluorescence imaging is an indispensable tool in life science research and medical diagnostics owing to its contributions to understanding cell physiology, transport characteristics, and interactions of ions, proteins, and other macromolecules.[1–6] Lasers, with their intense, narrow-band, and tunable emission, have paved the way for a variety of novel applications based on fluorescence imaging. However, the high coherence of the laser leads to the interference of light scattered from optical surfaces, dust particles, inherent imperfections in the system and the sample surface.[7] In wide-field imaging, these interference

[a]Centre for Optical and Laser Engineering (COLE), School of Mechanical and Aerospace Engineering, Nanyang Technological University, 50 Nanyang Avenue, 639798, Singapore. E-mail: mmurukeshan@ntu.edu.sg

[b]Department of Physics, Indian Institute of Technology Madras, Chennai, 600036, India. E-mail: cvijayan@iitm.ac.in

[c]Cognitive Neuroimaging Centre (CONIC), Nanyang Technological University, 59 Nanyang Drive, 636921, Singapore. E-mail: ppadmanabhan@ntu.edu.sg

[d]Department of Animal Science, Bharathidasan University, Tiruchirappalli, 620024, India

[e]Lee Kong Chian School of Medicine, Nanyang Technological University, 608232, Singapore

[f]Department of Clinical Neuroscience, Karolinska Institute, 17176 Stockholm, Sweden

† Electronic supplementary information (ESI) available. See DOI: 10.1039/d1na00866h

‡ These authors contributed equally to this work.

patterns and speckles caused by coherent lasers result in non-uniform illumination leading to the uneven excitation of fluorophores. This has been a cause of concern in the use of lasers for wide-field fluorescence imaging, particularly when quantitative measurements are involved.[8,9] For instance, in quantitative fluorescence imaging (qFI) techniques, the fluorescence intensity indicates the biomarker concentration that determines the status of a disease. It is even used to determine the tumour boundaries in fluorescence-image guided surgeries (FGS) in cancer therapy.[10,11] Hence, uniform excitation of the sample is of paramount importance in qFI techniques to obtain reliable fluorescence intensities. In order to avoid coherent artefacts, current wide-field microscopes use broadband light sources such as xenon arc lamps, mercury vapor lamps, and light emitting diodes (LEDs) that have low spatial coherence. Though these sources provide artefact-free uniform illumination, their photon degeneracy (the number of photons present in a small frequency window per unit area per unit time per unit solid angle per coherence volume) is quite low compared to lasers.[12,13] Hence, the samples under examination need to be exposed to high illumination fluxes to get bright fluorescence images. In specimens with more than one fluorophore, the larger bandwidth of these broadband sources causes increased spectral bleed-through and crossover of fluorescence emissions, affecting the analysis.[14]

To extend the benefits of the high photon degeneracy and narrow bandwidth of lasers to wide-field fluorescence imaging,

it is essential to reduce its spatial coherence. Several techniques such as phase randomisation using rotating diffusers, spatial light modulators, and nematic liquid crystal devices, vibrating multimode fibers, and scanning micromirrors are used to reduce the coherence of lasers.[15–21] However, all these are sequential decorrelation techniques that create time-varying independent speckle patterns, which are eventually averaged out by acquiring a large number of images. The long acquisition times required for reducing the speckle contrast to human perception level, the post-processing requirements, and the vibration noise introduced by the movement of mechanical parts restrict the usability of these techniques for real-time and *in vivo* wide-field fluorescence imaging applications and in cases that require dynamic imaging.[22,23] Hence alternative approaches to develop laser sources with low spatial coherence are essential.

Several methodologies have been proposed and illustrated to subdue the effect of the coherence of lasers by modifying the fundamental cavity design.[24–28] The geometry of the laser cavity determines the modes of lasing, spatial emission profile, and coherence properties. Hence, it is possible to control the coherence with modified cavity lasers.[29] Of particular interest is the random laser, in which highly scattering particles dispersed in a gain medium act as a cavity for trapping the light and provide sufficient feedback for lasing through multiple scattering.[30–36] The absence of a well-defined cavity and optic axis significantly reduces the mode competition, and all the randomly propagating modes contribute to the overall emission in random lasers, resulting in the drastic reduction of spatial coherence. Owing to their low spatial coherence, random lasers effectively reduce the speckle contrast instantaneously, and provide a good signal to noise ratio even in highly scattering environments.[37–39]

Biological samples are often highly diffusive, which lead to severe scattering, spatial cross talk, and coherent artefacts under conventional laser illumination. In this context, it is worthwhile to investigate the potential of random lasers for bioimaging applications. However, for random lasers to be used as an excitation source in fluorescence bioimaging, their gain must be increased as they typically have low emission intensities owing to the losses inherent to random lasing systems due to the absence of a well-defined cavity. Here, we use a plasmonic random laser with silver nanorod scatterers specifically designed for low threshold and bright lasing emission. The superior light scattering and field localization properties of plasmonic nanostructures are employed to effectively enhance the gain of the random lasing medium.[40–42] A wide-field fluorescence imaging system utilizing this spatially incoherent random laser is proposed for overcoming the limitations associated with coherent and broadband illuminations and is demonstrated in epi-illumination and trans-illumination microscopic configurations. Quantitative analysis of the image quality is carried out highlighting the advantages of the proposed technique.

Results and discussion

Anisotropic metal nanostructures possess broad plasmonic features due to multiple resonances, which can be utilized to achieve optimum spectral overlap with the gain medium in a random lasing system.[43–47] This can help in increasing the gain coupling without inducing substantial plasmonic losses. Here, we use one-dimensional silver nanostructures as the plasmonic scatterers as they offer better tunability and ease in fabrication among anisotropic structures. Further, the aspect ratio of these nanoscatterers can be tuned to obtain efficient scattering as well as localized surface plasmon resonance (LSPR) field enhancement, which will effectively reduce the lasing threshold. The aspect ratio optimization can be done using theoretical modelling and has been detailed in our previous work.[39] Based on the theoretical modelling, silver nanostructures with aspect ratio in the range 8.6 to 57.7 exhibit optimal scattering and LSPR properties for efficient random lasing in the designed system. Silver nanostructures in this aspect ratio range is synthesized and dispersed in rhodamine 6G (R6G) gain medium (see Methods section for details on the synthesis of nanostructures and the fabrication of random laser). Fig. 1a shows the normalised absorption spectrum of the synthesized silver nanorods and the
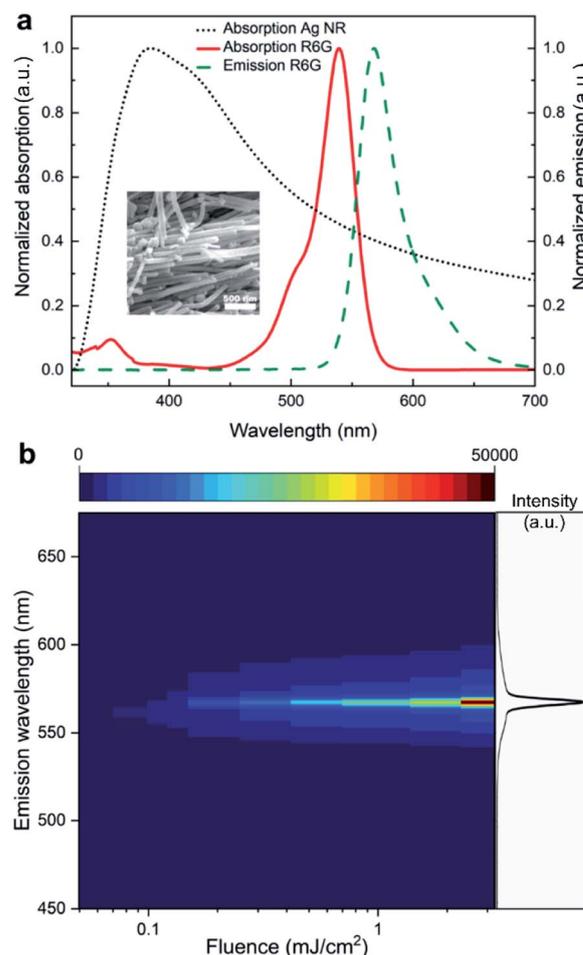
Fig. 1 (a) Normalised absorption spectra of the silver nanorods and rhodamine 6G and the emission spectrum of rhodamine 6G. Inset shows the SEM image of the silver nanorods. Scale bar represents 500 nm. (b) The evolution of random lasing emission with increasing pump fluence. The spectral profile of the emission at a pump fluence of 2.7 mJ cm^{-2} is shown on the right column.

normalized absorption and emission spectra of R6G dye. The SEM image of the synthesized silver nanorods is given in the inset. The nanorods have an absorption peak centered at 384 nm, which is quite well spaced away from the absorption and emission maxima of R6G. Nevertheless, owing to the anisotropic structure's broader resonance, a strong overlap is still maintained resulting in efficient gain coupling. As a result of the spectral and aspect ratio optimisations, an incoherent random lasing emission is achieved at a threshold as low as 0.116 mJ cm^{-2} (at 10 Hz repetition rate, this is equivalent to 11.6 µW mm^{-2}), at 567 nm wavelength with a linewidth of 5 nm. The emission profile of the random laser is shown in Fig. 1b, and the threshold characteristics are given in ESI Fig. S1.†

In order to demonstrate the proposed method, a random laser based wide-field fluorescence imaging system capable of trans- and epi-illumination imaging modes is developed. Fig. 2 shows the schematic illustration of the imaging system configuration (see Methods section for technical details). In bioimaging, the interpretations are highly reliant on the quality of the image, which is primarily determined by the resolution and contrast.[48] To evaluate the image quality offered by the developed system and to analyze the uniformity of the illumination profile, standard resolution test targets are first imaged by switching the system to bright-field microscopic mode (see Methods section for details). A 1951 USAF high-resolution test target (see ESI section S2†) and a Siemens star test target are used as the standard imaging samples for this purpose. We

compare the images recorded using the random laser illumination with the images obtained using a conventional laser and a broadband LED in the same experimental configuration under identical imaging conditions.

To ensure a fair comparison, the bandwidth of the broadband LED source is limited to 25 nm using an interference bandpass filter that is typically used in fluorescence microscopes. In addition, the illumination power density (illumination power/area) is kept to be the same at the imaging plane for all three sources (see Methods section for experimental details). Fig. 3a–c shows the central region of the Siemens star imaged using the LED, conventional laser, and random laser sources, respectively. The effect of coherent artefacts in wide-field imaging is evident from these images. The radius at the tip of the spokes of the Siemens star is 5.2 µm, which directly translates to a spatial frequency of 1102 line pairs (lp) per mm. Upon illumination using the LED (Fig. 3a) and the random laser (Fig. 3c), the tip of the spokes is distinctly visible, corresponding to a lateral resolution of 454 nm, which correlates well to the theoretical resolution limit of 432 nm for the system. On the other hand, with the conventional laser illumination, the spokes in the image are distorted near the center, obscuring the tip, due to coherent artefacts arising from the high degree of coherence of the conventional laser. The circular intensity profile close to the tip of the Siemens star, corresponding to a spatial frequency of 735 lp per mm (equivalent to a resolution of 680 nm, marked by the red circle in the inset), is shown in Fig. 3d. Further, the average contrast of the spokes and its standard deviation corresponding to the radially increasing spatial frequency are plotted in Fig. 3e. From the intensity profile and the contrast plots, it is evident that the artefacts caused by the high spatial coherence of the conventional laser distort the information contained in the image and limit the achievable resolution. The contrast is non-uniform in the image obtained with the conventional laser illumination and shows a spurious spike near the tip, due to the edge ringing artefact arising from its coherence.[49] In contrast, illumination using LED and random laser results in artefact-free images with similar intensity profile and contrast.

A statistical evaluation of the information preserved in the images captured using the three illumination sources is carried out to quantitatively assess the performance of the three sources. Considering each image as a matrix of scalar observables, it is possible to correlate these images with a reference image and establish a correlation coefficient, which gives the statistical measure of the linear dependence between the two matrices. We use the Pearson's correlation coefficient for this purpose, defined by,[50]
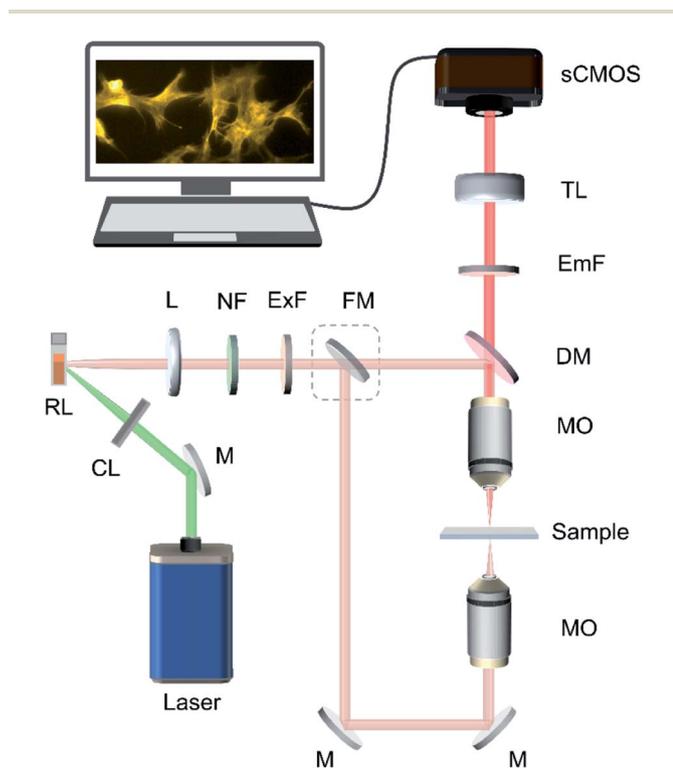

Fig. 2 Schematic illustration of the spatially incoherent random laser based wide-field fluorescence imaging system (M: mirror, CL: cylindrical lens, RL: random lasing sample, L: lens, NF: 532 nm notch filter, ExF: fluorescence excitation filter, FM: flip mirror, DM: dichroic mirror, MO: microscope objective, EmF: emission filter, TL: tube lens).

$$\text{Correlation coefficient} = \frac{\sum_i\sum_j(x_{ij}-\bar{x})(y_{ij}-\bar{y})}{\sqrt{\left(\sum_i\sum_j(x_{ij}-\bar{x})^2\right)\left(\sum_i\sum_j(y_{ij}-\bar{y})^2\right)}}$$

(1)

where, x_{ij} and y_{ij} are the individual sample points of the two matrices, which indicate the pixel content of the two images (X
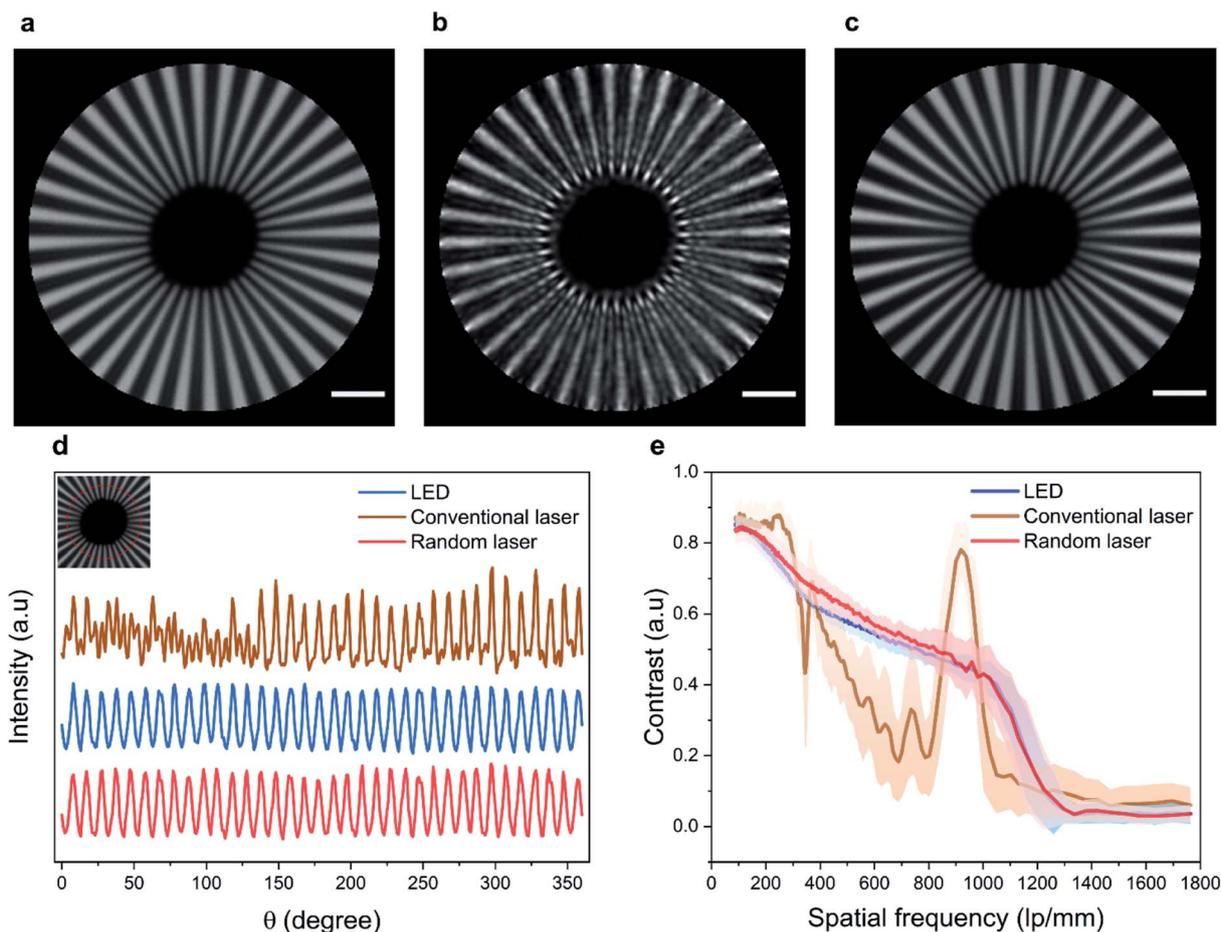
Fig. 3 Bright-field imaging of Siemens star test target to determine the resolution and image contrast using different illumination sources. (a) LED light source, (b) conventional laser source, (c) random laser source. (d) The circular intensity profile at the spatial frequency of 735 lp per mm (the intensity profiles are intentionally offset in the figures for clarity). The inset shows the central region of 20 μm × 20 μm and the red highlight denotes the circle corresponding to the spatial frequency of 735 lp per mm. (e) The plot showing the average contrast against spatial frequency with standard deviation shown as the shaded region. All scale bars represent 5 μm.

and Y), and $\bar{x}$ and $\bar{y}$ represent the sample mean. A correlation coefficient value of 1 indicates that both the images are identical implying that the evaluated image contains all of the information in the reference image.

For the evaluation, an image of the Siemens star recorded using a confocal microscope is used as the reference image. The Pearson's correlation coefficient calculated using eqn (1) for a region of 20 μm × 20 μm size at the center turns out to be 0.81 for the image obtained using the LED, 0.65 for the image obtained using the conventional laser, and 0.83 for the image obtained using the random laser. The presence of coherent artefacts leads to the poor correlation coefficient in the case of the conventional laser. Since the LED source and the random laser have low spatial coherence, images recorded with them are free of coherent artefacts and thus provide a higher correlation with the reference image. This further illustrates the role of the coherence of the illumination source on the image quality and resolution of the system. One of the state-of-the-art techniques to reduce the spatial coherence of conventional laser sources is to employ moving diffusers (often known as laser speckle

reducers). Images of the Siemens star test target recorded with the conventional laser illumination in combination with a laser speckle reducer are shown in ESI section S3† for comparison. In order to achieve an image quality equivalent to that offered by the random laser, around 1000 images need to be captured and averaged in this case.

These results show that the spatially incoherent random laser illumination can provide high-resolution, artefact-free images compared to conventional laser illumination. The contrast levels and correlation coefficient recorded with random laser and LED illumination suggest that their performances are identical in bright-field imaging mode. Also, this indicates that the comparison is done in a fair manner. When it comes to fluorescence imaging, the narrow spectrum and high photon degeneracy of the random laser are added advantages that help it to outperform LEDs. Random lasers are expected to provide specific and efficient excitation of fluorophores without spectral bleed through or fluorescence crossover. The unique combination of low spatial coherence with laser-like properties
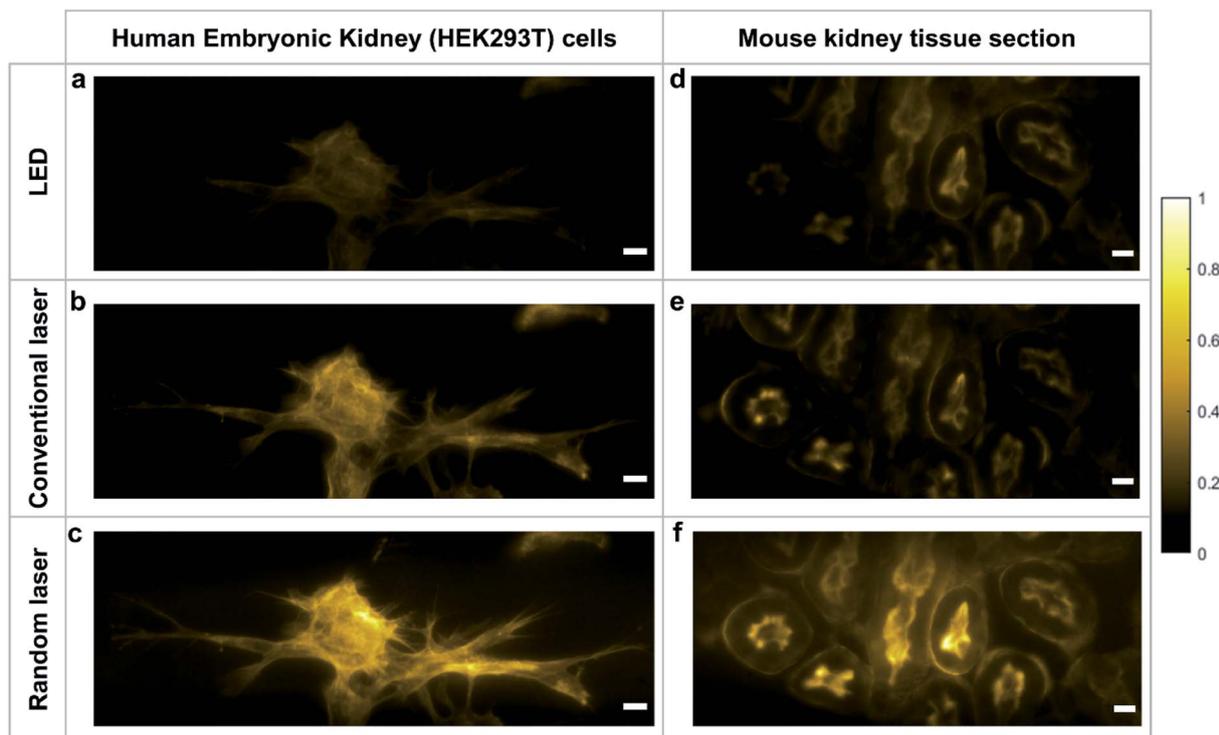
Fig. 4 Trans-illumination fluorescence bioimaging. Images of the monolayer human embryonic kidney cells (HEK293T) are shown in the first column and images of the mouse kidney section are shown in the second column. (a and d) LED illumination, (b and e) conventional laser illumination, (c and f) random laser illumination. All scale bars represent 10 μm.

makes the random laser a potential source for wide-field fluorescence bioimaging.

In order to evaluate the capability of the random laser for fluorescence bioimaging, a monolayer cell line of the human embryonic kidney (HEK293T) and a 16 μm thick tissue section of mouse kidney (both stained with Alexa fluor® 568 phalloidin; see Methods section for sample preparation details) are imaged using the random laser based wide-field fluorescence imaging system and the images are compared with those obtained using LED and conventional laser illumination in the same system. The illumination power density at the imaging plane is kept to be the same in all three cases and the images are captured under identical imaging conditions. The mouse kidney tissue section is a multilayered complex structure with large proteins, and hence is more diffusive compared to the monolayered HEK cell line. Initially, the specimens are imaged in trans-illumination geometry, by collecting the directly transmitted (bright-field images) and fluorescence emitted (fluorescence images) light in the transmission direction (see Methods section for details). ESI Fig. S4† shows the bright-field images of HEK cells, which also shows the quality of illumination rendered by each of the sources. The interference rings and speckles are evident in the images recorded with conventional laser illumination. On the contrary, the LED and random laser provide artefact-free illumination to the specimen and hence they are expected to excite the fluorophores evenly. The fluorescence images obtained by exciting the same sample location with LED, conventional laser, and random laser are shown in

Fig. 4a, b, and c, respectively. The image contrasts are evaluated for quantitative comparison and is found to be 0.65 for LED, 0.83 for conventional laser and 0.89 for random laser. The images of the mouse kidney section recorded with these sources shown in Fig. 4d–f also present a similar trend with a contrast of 0.71 for LED, 0.78 for conventional laser and 0.87 for random laser illumination.

In both samples, the images captured with the LED source are less bright than those captured with the laser sources. In fluorescence imaging, the emission intensity is highly dependent on the photon degeneracy and the spectral features of the illumination. LEDs by nature have low photon degeneracy and a broad emission spectrum. Even though the bandwidth of the LED was narrowed in these measurements using interference bandpass filters that are typically employed in fluorescence microscopes, the results show that it is still inefficient in exciting the fluorescent molecules when compared to a laser source. On the other hand, despite its high photon degeneracy and narrow bandwidth, conventional laser produces images with less contrast than the random laser. This is due to the non-uniform excitation rendered by the coherent artefacts that distorts the output. This reduces the overall intensity and affects the image quality, as observed.

Reflected light microscopy, also referred to as epi-illumination microscopy, is often the preferred mode for *in vivo* fluorescence imaging, especially in the case of thick or opaque samples.[51] Wide-field fluorescence imaging in epi-illumination mode is carried out to evaluate the potential of
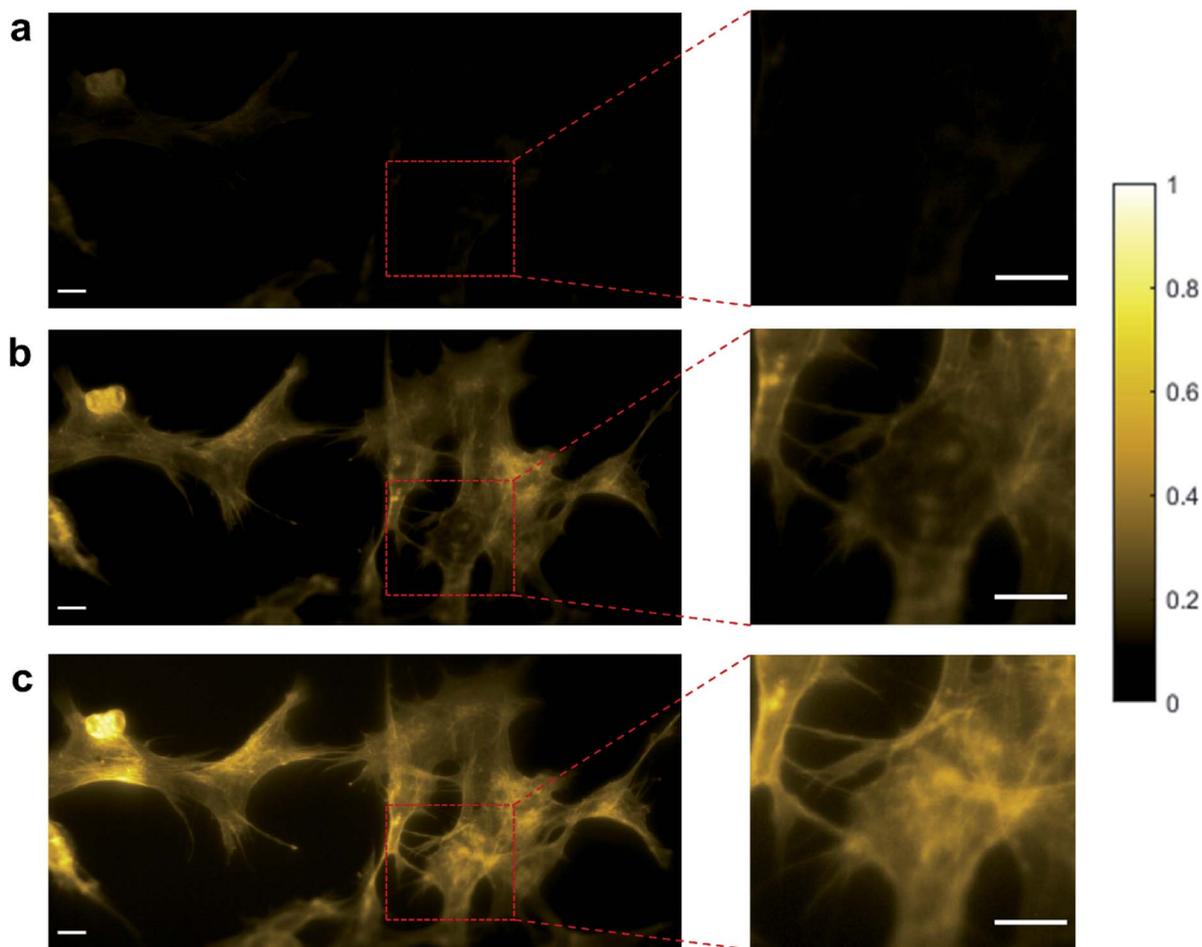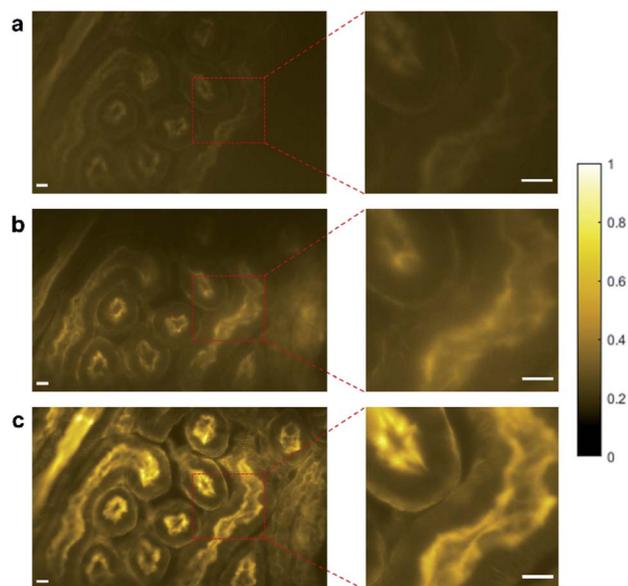
Fig. 5 Epi-illumination fluorescence bioimaging of HEK293T cells. Images of the monolayer human embryonic kidney cells (HEK293T) obtained using (a) LED illumination, (b) conventional laser illumination, and (c) random laser illumination. Enlarged view of the region marked by the red square in the images are shown on the right panel. All scale bars represent 10 μm.

random lasers for *in vivo* imaging applications. Fig. 5a–c shows the epi-fluorescence images of HEK cells and Fig. 6a–c shows the epi-fluorescence images of the mouse kidney section recorded with LED, conventional laser and random laser, respectively. Here also, for HEK293T cells, the image contrast is higher with random laser illumination (0.87) compared to LED (0.58) and conventional laser (0.81). A careful analysis of the image of the HEK cells captured with the conventional laser reveals that some of the structural details are missing when compared to the image obtained with the random laser. One such region with prominent difference is marked by the red square in the images (Fig. 5a–c) and their enlarged view is shown on the right panel. The images captured with conventional laser and random laser illumination are shown alternatingly for direct comparison in the video file attached in the ESI material.† The impairment caused by coherent illumination can be clearly seen in this video. This loss of information in the images recorded with the conventional laser source can be attributed to the uneven excitation caused by coherent artefacts. The same sample region of the HEK cells is imaged with the help of a laser speckle reducer in combination with the

conventional laser to verify whether this loss of information is indeed caused by coherent artefacts (see ESI section S5†). By averaging sufficient number of images in this scheme, the effect of coherence is reduced and eventually, the structural details became clearly visible as in the case of random laser based images. This confirms that coherent artefacts are responsible for the loss of information in the image recorded with conventional laser illumination. These coherent artefacts could be arising from the sample surface, or from the optical imperfections and multiple reflections in the optical components, or dust particles in the optical path. It should be noted that the presence of such artefacts from coherent illumination is not readily visible in fluorescence imaging due to the non-coherent nature of the fluorescence emission. This is why it is often not recognized to be a cause of concern in fluorescence imaging. However, this can lead to misinterpretation of the results, and miscalculations or errors in critical fluorescence imaging modalities such as quantitative fluorescence imaging and laser guided surgeries. It should also be noted that the noise and background fluorescence in the mouse kidney section sample are more pronounced in epi-illumination compared to trans-

Fig. 6 Epi-illumination fluorescence bioimaging of mouse kidney section. Images of the mouse kidney section obtained using (a) LED illumination, (b) conventional laser illumination, and (c) random laser illumination. Enlarged view of the region marked by the red square in the images are shown on the right panel. All scale bars represent 10 μm.

illumination geometry due to the high diffusivity of the sample. Nevertheless, the random laser illumination is capable of providing higher signal to noise ratio and better contrast (0.74) compared to the conventional laser (0.60) and LED (0.41) illuminations, even in such diffusive samples as evident from the images on the right panel of Fig. 6. A contrast enhancement of about 23% with the random laser illumination over the conventional laser illumination is achieved in the case of mouse kidney cells. Results from these measurements clearly illustrate the exemplary features of the random laser for high-resolution, artefact-free, wide-field fluorescence bioimaging. The advantage of the random laser source in fluorescence imaging comes from its laser like photon degeneracy and narrow spectrum, enabling efficient excitation, while the lack of spatial coherence reducing the coherent artefacts associated with conventional lasers. As a result, the fluorescence images obtained with random laser illumination exhibit the highest contrast. In short, the reduction in image quality is due to the coherent artefacts in the case of a conventional laser, and the low photon degeneracy and large bandwidth in the case of the LED source.

The random laser based wide-field fluorescence imaging scheme also presents other potential advantages such as time resolved imaging, owing to the short pulse nature and high photon degeneracy. The acquisition time for fluorescence imaging with the system described here is in the order of few seconds and is primarily limited due to the low repetition rate of the pump laser used (10 Hz). The repetition rate and pulse duration of random lasers are similar to that of their pump lasers.[52] Hence, it is possible to upgrade the system for faster image acquisition by the use of a high repetition rate pump

laser. In addition, due to the pulsed nature of the random laser excitation, and the nanosecond lifetime of the fluorophore (Alexa fluor® 568 phalloidin) emission, the actual exposure and image acquisition time duration would be of the order of a few microseconds.[53,54] The image acquisition time can further be shortened by incorporating an ICCD camera to enable even single shot imaging, potentially to a few nanoseconds.

The scheme described here can also be extended to other wide-field imaging techniques that benefits from laser illumination, such as the total internal reflection fluorescence (TIRF) microscopy and structured illumination microscopy (SIM). It is also noteworthy that the scheme described in this work uses a non-contact (WD = 0.66 mm), dry objective, which is advantageous for non-invasive, *in vivo* imaging applications. Further, the capability of the random laser for artefact-free imaging allows it to be used directly for bright-field imaging as well, wherein the conventional laser-based fluorescence microscopes generally rely on an auxiliary broadband source for bright-field imaging, especially to pan through the sample surface and for adjusting the focus. The use of a random laser source can thus enable homogenous illumination and faster switching between fluorescence and bright-field imaging modes, which are potentially useful for *in vivo* bioimaging and FGS. In contrast to LED sources, the narrow bandwidth of the random laser enables specific excitation of the fluorophore in samples consisting of multiple fluorophores, keeping bleed-through and background to a minimum, enabling better contrast imaging. The current drawback of random lasers is their relatively lower power densities due to low lasing efficiency, which may limit their application in samples with low fluorescence yield. However, recent advances in bright and electrically pumped random lasing systems demonstrate higher efficiencies and output powers.[55–57] Fluorescence microscopy systems utilizing such random laser sources for sample excitation present unique advantages such as high-resolution, real-time, non-contact, and *in vivo* imaging capabilities, producing exceptionally bright and artefact-free images.

Conclusions

We have proposed and demonstrated an artefact-free, wide-field fluorescence bioimaging system using a spatially incoherent plasmonic random laser. The bright plasmonic random laser with low threshold emission is fabricated using silver nanorod scatterers optimized for efficient scattering and field enhancement. The random laser combines the features such as narrow bandwidth emission and spectral control inherent to lasers with the spatial incoherence of broadband sources. Artefact-free illumination using the plasmonic random laser ensures uniform excitation of the specimen resulting in fluorescence images with superior contrast and sub-micron resolution, even in highly scattering and diffusive biological samples. Furthermore, this indicates its potential for quantitative assessment of fluorescence emission with high temporal resolution, which is otherwise challenging in bioimaging. With no additional mechanical moving parts or image processing required, the frame rate is limited only by the intensity of the random laser

source and the fluorophore efficiency. With the recent advances in high power, tunable, directional, and electrically pumped random lasers, we envisage that random lasers open up possibilities for developing highly competent wide-field fluorescence imaging systems with high spatial and temporal resolution for real-time, *in vivo* bioimaging.

Methods

Fabrication of plasmonic random laser

Materials. Ethylene glycol (EG) and silver nitrate ($AgNO_3$) from Merck life science Pvt Ltd, polyvinylpyrrolidone (PVP $M_w \sim$ 40 000) from Sisco Research Laboratories Pvt Ltd, sodium chloride G.R. (NaCl) from Burgoyne Burbidges & Co and rhodamine 6G from Lambda Physik are used as purchased.

Synthesis of silver nanorod scatterers. Based on the theoretical optimization, silver nanostructures with aspect ratio in the range 8.6 to 57.7 exhibits optimal scattering and LSPR properties, and are expected to show better lasing performance.[39] Silver nanorods in this aspect ratio range is synthesized *via* a solution based two-step injection polyol process.[58] Solutions of PVP (2005 g), and $AgNO_3$ (2.038 g) are prepared separately in 34 ml and 6 ml of EG, respectively. The PVP solution is heated to 160 °C under moderate stirring. 40 μl of 0.2 M NaCl solution is added to this. After one minute, $AgNO_3$ solution is added dropwise until the solution becomes cloudy and then the remaining $AgNO_3$ solution is added rapidly. The solution is maintained at 160 °C until it turns to glistening grey colour, which indicates the formation of silver nanostructures in the solution. The solution is then allowed to cool naturally to room temperature. It is centrifuged and the precipitate is washed several times with ethanol. It is then dried at 90 °C to yield silver nanorods in powder form. The TEM image, X-ray diffraction (XRD) pattern, and the size distribution of the synthesised nanorods are given in ESI section S6.†

Plasmonic random laser. The plasmonic random laser is fabricated by dispersing 12 mg of the synthesized nanorod scatterers and 12 mg of R6G dye in 2 ml ethylene glycol. The scatterer concentration is estimated to be of the order of $\sim 10^{11}$ particles per cm^3. This colloidal dispersion of R6G and Ag nanorods taken in a 1 cm quartz cuvette is optically pumped with a line focused second harmonic beam of an Nd:YAG laser (VIBRANT 355 II, OPOTEK Inc., 532 nm, 5 ns pulse width, 10 Hz repetition rate). The pumped area is evaluated to be 1.29 mm^2 using a Spiricon beam profiler CCD. The emission from the sample is analysed using a fibre optic spectrometer (Avantes, AvaSpec-ULS4096CL-EVO).

Fluorescence imaging system

All the images are recorded using a custom-built fluorescence microscope. The schematic of the random laser based wide-field fluorescence imaging system is shown in Fig. 2. The 532 nm pump laser, cylindrical lens, and colloidal dispersion of rhodamine 6G and Ag nanorods form the random laser source. Random laser emission is collected and collimated using a combination of lenses and is passed through a 532 nm notch

filter to remove the directly reflected pump beam from the cuvette surface. Any extraneous light in the emission is then filtered out using a fluorescence excitation filter (560 nm, 25 nm bandwidth, Edmund Optics). A flip mirror facilitates easy switching between trans-illumination and epi-illumination modes. The system can be set to epi-illumination imaging mode by removing the flip mirror from the beam path. The illumination beam is reflected by a dichroic mirror (MD588, Thorlabs) and focused onto the imaging sample by an infinity-corrected microscope objective lens (UMPlanFI, Olympus, 50×, dry, 0.8 numerical aperture (NA)). The imaging sample is mounted on an XYZ motorized translation stage (T-LS28M, Zaber Technologies) with sub-micron step resolution. In the epi-illumination geometry, the emitted fluorescence signals are collected by the same objective lens and then passed through the dichroic mirror, a fluorescence emission filter (MF630-69, Thorlabs) and a tube lens (TTL 200, Thorlabs), before it is fed to the sCMOS camera (Neo 5.5, Andor). With the flip mirror in place, the system is switched to trans-illumination mode, in which the sample is illuminated from the opposite side using another microscope objective (M Plan Apo, Mitutoyo, 50×, 0.55 NA).

Illumination power at the imaging plane is measured using a calibrated power sensor (S120VC, Thorlabs) connected to a power meter console (PM100A, Thorlabs). The power density is calculated by evaluating the area of illumination from the bright-field microscopic image. For comparison of the image quality, images are also captured by illuminating the sample with the LED source and the conventional laser source at the same wavelength and power density (2.02 μW mm^{-2}). For the LED illumination measurement, the random laser source is replaced with a white light LED (PSX501, Thorlabs) and the fluorescence excitation filter allows only 25 nm bandwidth light centered around 560 nm to reach the sample. For the conventional laser illumination measurement, a tunable pulsed laser (VIBRANT 355 II, OPOTEK Inc., 567 nm, 5 ns pulse width, 10 Hz repetition rate) is used. The spectra of the three illumination sources reaching the sample are shown in ESI Fig. S7.† All the fluorescence images presented in this paper are obtained by accumulating 10 images, each captured with 10 s exposure time. The fluorescence images are pseudo-colored using MATLAB®.

Bright-field imaging system

The spatial resolution of the system is evaluated in the bright-field microscopic imaging mode. For this purpose, the fluorescence emission filter is removed, and the dichroic mirror is replaced with a pellicle beam splitter (BP145B1, Thorlabs). This allows the reflected light from the sample to reach the sCMOS camera. A custom-made Siemens star (with 36 spokes) with maximum spatial frequency of 1102 lp per mm is used as the test target to evaluate the resolution of the system. The images of the Siemens star target shown in Fig. 3 are captured with 0.1 s exposure time (with single pulse illumination). The illumination power density used is 0.45 μW mm^{-2} for all the sources. To assess the image correlation coefficient, the reference image is captured using a commercial confocal microscope under white light

illumination (VK-X1000, Keyence, 150×, 0.95 NA). Bright-field images of HEK cell line are also captured in trans-illumination mode using the three illumination sources and the images obtained with 0.1 s exposure time are shown in ESI Fig. S4.†

Cell labelling for fluorescence bioimaging

Materials. DMEM-high glucose, Paraformaldehyde (PFA), Triton X-100, Bovine Serum Albumins (BSA), and poly L-lysine are purchased from Sigma Aldrich Co. LLC., and phosphate buffered saline (PBS), fetal bovine serum, penicillin/streptomycin and Alexa Fluor® 568 phalloidin are purchased from Thermo Fisher Scientific. FluorSave® mounting medium is purchased from EMD Millipore.

A monolayer cell line of the human embryonic kidney (HEK293T) and a 16 μm thick tissue section of mouse kidney, both stained with Alexa fluor® 568 phalloidin are used as specimens for fluorescence imaging. Alexa fluor® 568 phalloidin has excitation maximum at 578 nm and emission maximum at 600 nm (The random laser was specifically fabricated to have a lasing wavelength close to this excitation maximum). The mouse kidney section is purchased from Thermo Fisher Scientific (F24630, Fluocells prepared slide #3) and is used as received. The sample consists of a 16 μm thick cryo section of mouse kidney with its filamentous actin in glomeruli and the brush border stained with Alexa fluor® 568 phalloidin. The HEK293T cells are cultured in the laboratory using the following protocol.

Cell culture. Human embryonic kidney cells (HEK293T) are cultured in the DMEM-high glucose with 10% fetal bovine serum, 1% penicillin/streptomycin. The cells are incubated in 5% CO_2 humidified incubator at 37 °C. The cultured cell of passages < 10 are used in the experiments.

Alexa Fluor® 568 phalloidin staining. Cover slips are treated with poly L-lysine and is exposed to UV radiation. Approximately 1×10^5 HEK293T cells are seeded in 6 wells tissue-culture plates. On the next day, the cells are fixed with 4% PFA for 10 minutes and washed thrice with 1× PBS (5 minutes per wash). The cells are permeabilized with 0.1% Triton X-100 in PBS (PBST) for 10 minutes at room temperature and the cells are washed with 1× PBS (5 minutes per wash). Later, the cells were treated with 0.5 N HCl for 10 minutes at room temperature to retrieve the masked antigens and washed thrice using PBST (5 minutes per wash). The cells are blocked with 1× BSA (prepared in PBST) for 1 hour at room temperature to avoid the background fluorescence. The Alexa Fluor® 568 phalloidin stock solution (400×) is prepared in DMSO and the working solutions are prepared in 1× PBS. The cells are stained with 15× working phalloidin for 45 minutes at room temperature and washed twice with 1× PBS for 5 minutes each. Finally, the DAPI nuclear stain is added in PBS for 5 minutes and washed thrice with 1× PBS (5 minutes per wash). The cover slips are mounted on glass slides using FluorSave® mounting medium for microscopy analysis. The fluorescence image of the sample recorded using a commercial laser scanning confocal microscope (LSM800, Zeiss) with 63× oil immersion objective of 1.4 NA is shown in ESI Fig. S8.†

Author contributions

R. G. and C. S. S. S. contributed equally to this work. R. G., C. S. S. S., C. V., and V. M. M. conceived the idea. R. G. and C. S. S. S. designed the system and performed the experiments. V. S. G. assisted in the random laser fabrication. R. M. A. and P. P. designed the fluorescence labelling protocols and prepared the biosamples. P. P. and B. G. supervised the biosample synthesis and provided the facilities. R. G. analyzed the data and performed the calculations and image analysis. R. G. and C. S. S. S. wrote the first version of the manuscript. All authors contributed to the discussion, writing, and editing of the manuscript. C. V. and V. M. M. supervised the overall project under NTU-IITM joint-degree program.

Conflicts of interest

The authors declare no conflicts of interest.

Acknowledgements

Notes and references

1 N. Jiang, J. Fan, F. Xu, X. Peng, H. Mu, J. Wang and X. Xiong, *Angew. Chem., Int. Ed.*, 2015, **54**, 2510–2514.

2 A. Shinde, S. M. Perinchery and V. M. Murukeshan, *Sci. Rep.*, 2017, **7**, 1–8.

3 J. Capoulade, M. Wachsmuth, L. Hufnagel and M. Knop, *Nat. Biotechnol.*, 2011, **29**, 835–839.

4 S. M. Perinchery, A. Shinde and M. V. Matham, *Biomed. Opt. Express*, 2016, **7**, 5308.

5 J. Leslie, S. M. Robinson, F. Oakley and S. Luli, *Sci. Rep.*, 2021, **11**, 1415.

6 C. S. Suchand Sandeep, S. Sarangapani, X. J. J. Hong, T. Aung, M. Baskaran and V. M. Murukeshan, *J. Biophotonics*, 2019, **12**, e201900048.

7 J. W. Goodman, *Speckle Phenomena in Optics: Theory and Applications*, SPIE Press, Washington, 2nd edn, 2020.

8 J. C. Waters, *J. Cell Biol.*, 2009, **185**, 1135–1148.

9 S. Tayal, V. Singh, T. Kaur, N. Singh and D. S. Mehta, *Methods Appl. Fluoresc.*, 2020, **8**, 035004.

10 G. M. van Dam, G. Themelis, L. M. A. Crane, N. J. Harlaar, R. G. Pleijhuis, W. Kelder, A. Sarantopoulos, J. S. de Jong,

H. J. G. Arts, A. G. J. van der Zee, J. Bart, P. S. Low and V. Ntziachristos, *Nat. Med.*, 2011, **17**, 1315–1319.

11 P. A. Valdes, V. L. Jacobs, B. C. Wilson, F. Leblond, D. W. Roberts and K. D. Paulsen, *Opt. Lett.*, 2013, **38**, 2786.

12 L. Mandel, *J. Opt. Soc. Am.*, 1961, **51**, 797.

13 L. Mandel and E. Wolf, *Optical Coherence and Quantum Optics*, Cambridge University Press, Cambridge, 1995.

14 T. Zimmermann, in *Microscopy Techniques, Advances in Biochemical Engineering*, ed. J. Rietdorf, Springer, Berlin, 2005, vol. 95, pp. 245–265.

15 R. Hard, R. Zeh and R. D. Allen, *J. Cell Sci.*, 1977, **23**, 335–343.

16 S. Lowenthal and D. Joyeux, *J. Opt. Soc. Am.*, 1971, **61**, 847.

17 H. Ambar, Y. Aoki, N. Takai and T. Asakura, *Appl. Phys. B: Photophys. Laser Chem.*, 1985, **38**, 71–78.

18 T. Stangner, H. Zhang, T. Dahlberg, K. Wiklund and M. Andersson, *Appl. Opt.*, 2017, **56**, 5427.

19 M. N. Akram, Z. Tong, G. Ouyang, X. Chen and V. Kartashov, *Appl. Opt.*, 2010, **49**, 3297.

20 D. J. Hansford, J. A. J. Fells, S. J. Elston and S. M. Morris, *Appl. Phys. Lett.*, 2016, **109**, 261104.

21 H. Farrokhi, T. M. Rohith, J. Boonruangkan, S. Han, H. Kim, S.-W. Kim and Y.-J. Kim, *Sci. Rep.*, 2017, **7**, 15318.

22 S. D. Silverstein and M. O'Donnell, *J. Opt. Soc. Am. A*, 1988, **5**, 104.

23 S. Roelandt, Y. Meuret, A. Jacobs, K. Willaert, P. Janssens, H. Thienpont and G. Verschaffelt, *Opt. Express*, 2014, **22**, 23965.

24 L. Xu, Y. Wang, Y. Jia and W. Zheng, *Opt. Lett.*, 2020, **45**, 5097.

25 R. Chriki, M. Nixon, V. Pal, C. Tradonsky, G. Barach, A. A. Friesem and N. Davidson, *Opt. Express*, 2015, **23**, 12989.

26 M. Nixon, B. Redding, A. A. Friesem, H. Cao and N. Davidson, *Opt. Lett.*, 2013, **38**, 3858.

27 B. Redding, A. Cerjan, X. Huang, M. L. Lee, A. D. Stone, M. A. Choma and H. Cao, *Proc. Natl. Acad. Sci.*, 2015, **112**, 1304–1309.

28 K. Kim, S. Bittner, Y. Zeng, S. F. Liew, Q. Wang and H. Cao, *Appl. Phys. Lett.*, 2019, **115**, 071101.

29 H. Cao, R. Chriki, S. Bittner, A. A. Friesem and N. Davidson, *Nat. Rev. Phys.*, 2019, **1**, 156–168.

30 Y.-J. Lee, C.-Y. Chou, Z.-P. Yang, T. B. H. Nguyen, Y.-C. Yao, T.-W. Yeh, M.-T. Tsai and H.-C. Kuo, *Nanoscale*, 2018, **10**, 10403–10411.

31 D. S. Wiersma, *Nat. Photonics*, 2013, **7**, 188–196.

32 Y. J. Lee, T. W. Yeh, Z. P. Yang, Y. C. Yao, C. Y. Chang, M. T. Tsai and J. K. Sheu, *Nanoscale*, 2019, **11**, 3534–3545.

33 B.-H. Li, C.-X. Shan, D.-Z. Shen, H.-A. Ma, J.-M. Qin, X.-P. Jia, Y.-J. Lu, Y.-L. Wang, Z.-H. Chen and Z.-X. Zhou, *Optica*, 2015, **2**, 558–562.

34 B. H. Hokr, J. N. Bixler, M. T. Cone, J. D. Mason, H. T. Beier, G. D. Noojin, G. I. Petrov, L. A. Golovan, R. J. Thomas, B. A. Rockwell and V. V. Yakovlev, *Nat. Commun.*, 2014, **5**, 1–5.

35 Y. Bian, X. Shi, M. Hu and Z. Wang, *Nanoscale*, 2020, **12**, 3166–3173.

36 B. Xu, Z. Gao, Y. Wei, Y. Liu, X. Sun, W. Zhang, X. Wang, Z. Wang and X. Meng, *Nanoscale*, 2020, **12**, 4833–4838.

37 B. Redding, M. A. Choma and H. Cao, *Nat. Photonics*, 2012, **6**, 355–359.

38 T.-H. Yang, C.-W. Chen, H.-C. Jau, T.-M. Feng, C.-W. Wu, C.-T. Wang and T.-H. Lin, *Appl. Phys. Lett.*, 2019, **114**, 191105.

39 R. Gayathri, K. Monika, V. M. Murukeshan and C. Vijayan, *Opt. Laser Technol.*, 2021, **139**, 106959.

40 S. Lee, Y.-C. Lim, H. Kim, D. H. Seo, J. Na, H. Kim, K. T. Nam and Y. Jeong, *ACS Photonics*, 2022, **9**, 613–620.

41 S. F. Haddawi, H. R. Humud, S. A. Monfared and S. M. Hamidi, *Waves Random Complex Media*, 2021, DOI: 10.1080/17455030.2021.1943563.

42 J. Zhang, Z. Li, Y. Bai and Y. Yin, *Appl. Mater. Today*, 2022, **26**, 101358.

43 C. J. Murphy, T. K. Sau, A. M. Gole, C. J. Orendorff, J. Gao, L. Gou, S. E. Hunyadi and T. Li, *J. Phys. Chem. B*, 2005, **109**, 13857–13870.

44 V. S. Gummaluri, R. Gayathri, C. Vijayan and V. M. Murukeshan, *J. Opt.*, 2020, **22**, 065003.

45 T. Zhai, J. Chen, L. Chen, J. Wang, L. Wang, D. Liu, S. Li, H. Liu and X. Zhang, *Nanoscale*, 2015, **7**, 2235–2240.

46 S. Bhaskar, A. K. Singh, P. Das, P. Jana, S. Kanvah, S. Bhaktha B N and S. S. Ramamurthy, *ACS Appl. Mater. Interfaces*, 2020, **12**, 34323–34336.

47 S. Bhaskar, P. Das, V. Srinivasan, S. B. N. Bhaktha and S. S. Ramamurthy, *Mater. Res. Bull.*, 2022, **145**, 111558.

48 M. J. Sanderson, I. Smith, I. Parker and M. D. Bootman, *Cold Spring Harb. Protoc.*, 2014, **2014**, 1042–1065.

49 P. S. Considine, *J. Opt. Soc. Am.*, 1966, **56**, 1001.

50 A. G. Asuero, A. Sayago and A. G. González, *Crit. Rev. Anal. Chem.*, 2006, **36**, 41–59.

51 J. James and H. J. Tanke, *Biomedical Light Microscopy*, Springer Netherlands, Dordrecht, 1991.

52 X. Shi, Q. Chang, J. Tong, Y. Feng, Z. Wang and D. Liu, *Sci. Rep.*, 2017, **7**, 1–8.

53 T. Gajdos, B. Hopp and M. Erdélyi, *J. Fluoresc.*, 2020, **30**, 437–443.

54 A. Hartmann, F. Berndt, S. Ollmann, G. Krainer and M. Schlierf, *J. Chem. Phys.*, 2018, **148**, 123330.

55 B. H. Hokr, J. N. Bixler, M. T. Cone, J. D. Mason, H. T. Beier, G. D. Noojin, G. I. Petrov, L. A. Golovan, R. J. Thomas, B. A. Rockwell and V. V. Yakovlev, *Nat. Commun.*, 2014, **5**, 4356.

56 S. Chu, G. Wang, W. Zhou, Y. Lin, L. Chernyak, J. Zhao, J. Kong, L. Li, J. Ren and J. Liu, *Nat. Nanotechnol.*, 2011, **6**, 506–510.

57 S. F. Yu, *J. Phys. D: Appl. Phys.*, 2015, **48**, 483001.

58 M. Hu, J. Gao, Y. Dong, S. Yang and R. K. Y. Li, *RSC Adv.*, 2012, **2**, 2055.